A Study on Penetration Fracture Characteristics of Glass Plates Subjected to Impact Loadings

Kwang-Hee Im*, Ji-Hoon Kim and In-Young Yang*****

(Received November 30, 1996)

In this study, a comparison between theoretical solutions and experimental results are examined for fracture conditions in the case of float glass plates subject to static loadings. The ranges from fracture-generated initiations to critical penetration energies are confirmed according to the impactor mass under high velocity, and an analytical method is presented to determine the fracture strength and penetration strength. Also, fracture patterns are investigated according to impact velocities.

Key Words: Impact Energy, Critical Penetration Energy, Glass Plates, Steel Ball, High Speed Impact, Fracture Strength

1. Introduction

When a machine or structural component is subjected to impact loading, unexpected failure can occur as a result of stress wave effects. Such impact problems are dependent on dynamic behavior, and to investigate the dynamic phenomena generated in the materials, research activities have recently focused on plates subjected to high-speed impact (Wang et al., 1989 and Holian, 1990), on the impact of composite shell members used in ships and aircraft bodies (Chao et al., 1989), and on impact problems invoiving structural members (Kishimoto et al., 1989).

Clearly impact strength needs to be analyzed in relation to impact problems of plates (Ujihash et al., 1986), which are widely used in structural plate members. The fracture patterns are especially diverse in the case of fragile materials such as bus and building glasses subjected to the impact of high-speed flying bodies, and it is difficult for fracture phenomena to be analyzed quantitatively.

Recently TV structures have been improved through impact test, which is carried out to devise a safety measure of fracture prevention for a TV Braun tube (Kim et al., 1993, Hondou et al., 1978 and Ganebasi et al., 1993) and through a photoelasticity test to obtain the impact stress distribution through a steel drop test. But experimental result strength has not been analyzed over the fracture strength and critical penetration energy. The fracture patterns are diverse even though the conditions are the same, so the fracture mechanism needs to be analyzed.

Thus, in this study, when float glass plates are subjected to static loading, the fracture patterns are observed until failure of the glasses occurs, and the measured strain is compared with numerically calculated solutions. In the case of glass plates subjected to the high speed impact, the limit and critical penetration energy ranges are obtained according to the dimensions of impactor mass. An analytical method is presented to analyze the fracture and penetration strength, and the fracture patterns are investigated with respect to impact speed.

* Graduate Student, Department of Mechanical Engineering, Chosun University 375 Sosok-dong, Dong-gu, Kwangju 501-759, Korea

** Graduate Student, Department of Mechanical Design Engineering, Chosun University 375 Sosok-dong, Dong-gu, Kwangju 501-759, Korea

*** Factory Automation Center for Parts of Vechicles, Department of Mechanical Design Engineering, Chosun University 375 Sosok-dong, Dong-gu, Kwangju 501-759, Korea

For each test, the static and impact loads are applied to the center zone of a square plate (300×300 mm) supported at its edges. The three-dimensional dynamic theory of elasticity using Cartesian coordinates and displacement potential theory (Nakahara, 1979) is used and impact stresses are analyzed. When a ball collides with an infinite plate, Hertzian contact theory (Goldsmith, 1990) is applied to this study. The numerical inverse Laplace transform uses an F. F. T. algorithm, with the parameter of the Laplace transform is zero for static strength analysis.

2. Theoretical Analysis

2.1 Stress analysis

In the case where the center zone of a square plate (2a 2a) simply supported at four sides is subjected to partial distributed impact loading qof(t) as shown in Fig. 1, the impulsive stresses generated can be analyzed (Yang, 1988) by using the three-dimensional dynamic theory of elasticity (Johnson, 1972).

The origin point of coordinates (x, y, z) is at the center of the middle plane of plate. At the origin, let us now represent u, v, w, σ_x, σ_y, σ_z, and τ_{xy}, τ_{xz}, τ_{yz} as the displacement components, the normal stresses, and the shear stress components, respectively. The three-dimensional equations of motion are (Johnson, 1972).:

$$\frac{\partial\sigma_x}{\partial x}+\frac{\partial\tau_{yx}}{\partial y}+\frac{\partial\tau_{zx}}{\partial z}=\rho\frac{\partial^2u}{\partial t^2}$$
$$\frac{\partial\tau_{xy}}{\partial x}+\frac{\partial\sigma_y}{\partial y}+\frac{\partial\tau_{zy}}{\partial z}=\rho\frac{\partial^2v}{\partial t^2}$$
$$\frac{\partial\tau_{xz}}{\partial x}+\frac{\partial\tau_{yz}}{\partial y}+\frac{\partial\sigma_z}{\partial z}=\rho\frac{\partial^2w}{\partial t^2} \tag{1}$$

Substituting for stress-strain and strain-displacement relations into Eq. (1) leads to the displacement equations (Ni, 1985):

$$\nabla^2u+\frac{1}{1-2\nu}\frac{\partial e}{\partial x}=\frac{\rho}{G}\frac{\partial^2u}{\partial t^2}$$
$$\nabla^2v+\frac{1}{1-2\nu}\frac{\partial e}{\partial y}=\frac{\rho}{G}\frac{\partial^2v}{\partial t^2}$$
$$\nabla^2w+\frac{1}{1-2\nu}\frac{\partial e}{\partial z}=\frac{\rho}{G}\frac{\partial^2w}{\partial t^2} \tag{2}$$

where

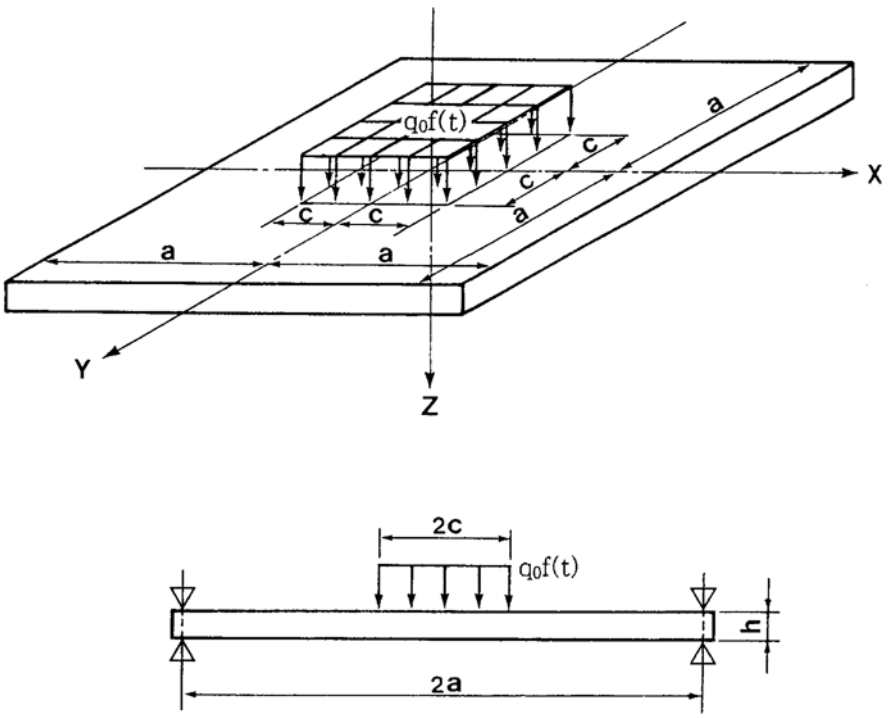

Fig. 1 A square plate subjected to partial distributed impact load on the center

$$e=\frac{\partial u}{\partial x}+\frac{\partial v}{\partial y}+\frac{\partial w}{\partial z},$$
$$\nabla^2=\frac{\partial^2}{\partial x^2}+\frac{\partial^2}{\partial y^2}+\frac{\partial^2}{\partial z^2}$$

Here, G is the shear elastic modulus.

The displacement components can be represented in terms of displacement potentials (φ_0, λ_1, λ_2, λ_3) (Nakahara, 1979 and Achenbach, 1975) as follows:

$$2Gu=\frac{\partial\varphi_0}{\partial x}+\frac{\partial\lambda_3}{\partial y}-\frac{\partial\lambda_2}{\partial z}$$
$$2Gv=\frac{\partial\varphi_0}{\partial y}+\frac{\partial\lambda_1}{\partial z}-\frac{\partial\lambda_3}{\partial x}$$
$$2Gw=\frac{\partial\varphi_0}{\partial z}+\frac{\partial\lambda_2}{\partial x}-\frac{\partial\lambda_1}{\partial y} \tag{3}$$

Substitution of Eq. (3) into Eq. (2) yields the governing wave equations from the potentials as:

$$\nabla^2\varphi_0=\frac{1}{c_p^2}\frac{\partial^2\varphi_0}{\partial t^2},\ \nabla^2\lambda_1=\frac{1}{c_s^2}\frac{\partial^2\lambda_1}{\partial t^2},\ \nabla^2\lambda_2=\frac{1}{c_s^2}\frac{\partial^2\lambda_2}{\partial t^2} \tag{4}$$

where $c_p{}^2=\frac{2(1-\nu)}{1-2\nu}\frac{G}{\rho}$, $c_s{}^2=\frac{G}{\rho}$

Here, ν is Poisson's ratio of the plate, cp is the propagation velocity of the longitudinal wave, and cs is the propagation velocity of the shear wave.

These displacement potentials can be approximately given by:

$$\varphi_0=\Phi_{mn}\cos\alpha_m x\cos\alpha_n y,$$
$$\lambda_1=\Delta^1{}_{mn}\cos\alpha_m x\sin\alpha_n y$$
$$\lambda_2=\Delta^2{}_{mn}\sin\alpha_m x\cos\alpha_n y,$$
$$\lambda_3=\Delta^3{}_{mn}\sin\alpha_m x\cos\alpha_n y \tag{5}$$

where $\alpha_m=\frac{\pi(2m-1)}{2a}$, $\alpha_n=\frac{\pi(2n-1)}{2a}$ ($m,\ n=1, 2, \ldots$)

and Φ_{mn}, $\Delta^1{}_{mn}$, $\Delta^2{}_{mn}$, $\Delta^3{}_{mn}$ are functions having two undetermined coefficients at the general solutions.

Here, in the absence of Z-directional rotation, $\lambda_3=0$.

The use of the stress-strain and strain displacement relation in Eq. (3) leads to the following relations of the stress components and displacement potentials:

$$\sigma_x=\frac{\partial^2\varphi_0}{\partial x^2}-\frac{\partial^2\lambda_2}{\partial x\partial z}+\frac{\nu}{1-2\nu}\nabla^2\varphi_0$$
$$\sigma_y=\frac{\partial^2\varphi_0}{\partial y^2}-\frac{\partial^2\lambda_1}{\partial y\partial z}+\frac{\nu}{1-2\nu}\nabla^2\varphi_0$$
$$\sigma_z=\frac{\partial^2\varphi_0}{\partial z^2}+\frac{\partial^2\lambda_2}{\partial x\partial z}-\frac{\partial^2\lambda_1}{\partial z\partial y}+\frac{\nu}{1-2\nu}\nabla^2\varphi_0 \tag{6}$$
$$\tau_{xy}=\frac{\partial^2\varphi_0}{\partial x\partial z}+\frac{1}{2}\left(\frac{\partial^2\lambda_1}{\partial x\partial z}-\frac{\partial^2\lambda_2}{\partial y\partial z}\right)$$
$$\tau_{xz}=\frac{\partial^2\varphi_0}{\partial x\partial z}+\frac{1}{2}\left(\frac{\partial^2\lambda_2}{\partial x^2}-\frac{\partial^2\lambda_1}{\partial x\partial y}-\frac{\partial^2\lambda_2}{\partial z^2}\right)$$
$$\tau_{yz}=\frac{\partial^2\varphi_0}{\partial y\partial z}+\frac{1}{2}\left(\frac{\partial^2\lambda_2}{\partial x\partial y}-\frac{\partial^2\lambda_1}{\partial y^2}-\frac{\partial^2\lambda_1}{\partial z^2}\right)$$

Because Eq. (4) are linear differential equations, we can remove time t by applying the Laplace transform.

The initial conditions for the displacement potentials on a square plate before impact ($t\leq 0$) can be expressed as:

$$(u,\ v,\ w)_{t=0}=0,\ \left(\frac{\partial u}{\partial t},\ \frac{\partial v}{\partial t},\ \frac{\partial w}{\partial t}\right)_{t=0}=0 \tag{7}$$

The Laplace transform applied to Eq. (4) gives:

$$\nabla^2\bar{\varphi}_0=\frac{p^2}{c_p{}^2}\bar{\varphi}_0,\ \nabla^2\bar{\lambda}_1=\frac{p^2}{c_s{}^2}\bar{\lambda}_1,\ \nabla^2\bar{\lambda}_2=\frac{p^2}{c_s{}^2}\bar{\lambda}_2 \tag{8}$$

where $\bar{\varphi}_0=\int_0^\infty\varphi_0 e^{-pt}dt$, $\bar{\lambda}_1=\int_0^\infty\lambda_1 e^{-pt}dt$,
$\bar{\lambda}_2=\int_0^\infty\lambda_2 e^{-pt}dt$

p is the Laplace parameter and symbol ($\bar{}$) means Laplace transform.

Substitution of Eq. (4) into Eq. (8) leads to the following ordinary differential equations for Z-direction behavior:

$$\frac{d^2\bar{\Phi}_{mn}}{dz^2}=(\alpha_m{}^2+\alpha_n{}^2+\frac{p^2}{c_1{}^2})\bar{\Phi}_{mn}$$
$$\frac{d^2\bar{\Delta}^1{}_{mn}}{dz^2}=(\alpha_m{}^2+\alpha_n{}^2+\frac{p^2}{c_2{}^2})\bar{\Delta}^1{}_{mn}$$
$$\frac{d^2\bar{\Delta}^2{}_{mn}}{dz^2}=(\alpha_m{}^2+\alpha_n{}^2+\frac{p^2}{c_2{}^2})\bar{\Delta}^2{}_{mn} \tag{9}$$

General solutions of Eq. (4) can now be represented as:

$$\bar{\varphi}_0=\sum_{m=1}^{\infty}\sum_{n=1}^{\infty}[C_1e^{\beta_{mn}z}+C_2e^{-\beta_{mn}z}]\cos\alpha_m x\cos\alpha_n y$$
$$\bar{\lambda}_1=\sum_{m=1}^{\infty}\sum_{n=1}^{\infty}[D_1e^{\gamma_{mn}z}+D_2e^{-\gamma_{mn}z}]\cos\alpha_m x\sin\alpha_n y$$
$$\bar{\lambda}_2=\sum_{m=1}^{\infty}\sum_{n=1}^{\infty}[E_1e^{\gamma_{mn}z}+E_2e^{-\gamma_{mn}z}]\sin\alpha_m x\cos\alpha_n y \tag{10}$$

Here,

$$\beta_{mn}^2=\alpha_m^2+\alpha_n^2+\frac{p^2}{c_1^2},\ \gamma_{mn}^2=\alpha_m^2+\alpha_n^2+\frac{p^2}{c_2^2}$$

and C_1, C_2, D_1, D_2, E_1, E_2 are unknown coefficients to be determined by boundary conditions. The boundary conditions can be expressed as follows (see Fig. 1):

(i) $\tau_{zx}=\tau_{zy}=0$ at $Z=-h/2$ (upper side of plate)

$$\sigma_z=-q_0 f(t)\,U(c-|x|)\,U(c-|y|) \quad (11)$$

(ii) $\sigma_z=\tau_{zx}=\tau_{zy}=0$ at $Z=h/2$ (lower side of plate)

where $U(c-|x|)\,U(c-|y|)$ denotes the unit step funtion.

The Laplace transform of Eq. (11) becomes

(i) $\bar{\sigma}_z=-q_0\bar{f}(p)\,U(c-|x|)\,U(c-|y|)$, $\bar{\tau}_{xz}=\tau=0$ at $Z=-h/2$

(ii) $\bar{\sigma}_z=\bar{\tau}_{xz}=\bar{\tau}_{zy}=0$ at $Z=h/2$ (12)

After substituting Eq. (10) into the Eq. (6), and the boundary condition (12) into Eq. (6), we can determine the unknown coefficients (C_1, C_2, D_1, D_2, E_1, E_2).

However, in the expression for σ_z the right-hand side denotes a periodic function and the left term implies a unit step function. Therefore the Fourier cosine transform of $U(c-|x|)\,U(c-|y|)$ can be utilized, and the result is as follows:

$$\begin{aligned}\bar{\sigma}_z=&\sum_{m=1}^{\infty}\sum_{n=1}^{\infty}[\beta_{mn}^2 e^{(-\beta_{mn}Z/2)}C_1+\beta_{mn}^2 e^{(\beta_{mn}Z/2)}C_2\\&-\alpha_n\beta_{mn}e^{(-\beta_{mn}Z/2)}D_1+\alpha_n\beta_{mn}e^{(-\beta_{mn}Z/2)}D_2\\&+\beta_{mn}\alpha_m e^{(-\beta_{mn}Z/2)}E_1-\beta_{mn}\alpha_m e^{(\beta_{mn}Z/2)}E_2]\\=&-q_0\bar{f}(t)\sum_{m=1}^{\infty}\sum_{n=1}^{\infty}\frac{4\sin(\alpha_m c)\sin(\alpha_n c)}{\alpha_m\alpha_n a^2}\end{aligned} \quad (13)$$

The area $(2c\times 2c)$ of partially distributed loading can be made to approach zero by making the right-hand side of Eq. (13) be a concentrated loading. That is, let F0 be the concentrated load acting on the plate (Yang, 1988):

$$\lim_{c\to 0}4q_0c^2\frac{\sin(\alpha_m c)\sin(\alpha_n c)}{a^2(\alpha_m c)(\alpha_n c)}=\frac{F_0}{a^2},$$
$$F_0=4c^2q_0 \quad (14)$$

Obtaining simultaneous equations of sixth degree using the foregoing equation, one can determine the unknown coefficients (C_1, C_2, D_1, D_2, E_1, E_2). Subjequenthy, substituting these equations into Eq. (10) leads to the stress-component equations as follows:

$$\begin{aligned}\bar{\sigma}_x=&\sum_{m=1}^{\infty}\sum_{n=1}^{\infty}[(-\alpha_m^2+\frac{\nu}{1-2\nu}\frac{p^2}{c_1^2})e^{\beta_{mn}Z}C_1\\&+(-\alpha_m^2+\frac{\nu}{1-2\nu}\frac{p^2}{c_1^2})e^{-\beta_{mn}Z}C_2-\alpha_m\gamma_{mn}E_1e^{\gamma_{mn}Z}\\&+\alpha_m\gamma_{mn}e^{-\gamma_{mn}Z}E_2]\cos\alpha_m x\cos\alpha_n y\\\bar{\sigma}_y=&\sum_{m=1}^{\infty}\sum_{n=1}^{\infty}[(-\alpha_n^2+\frac{\nu}{1-2\nu}\frac{p^2}{c_1^2})e^{\beta_{mn}Z}C_1\\&+(-\alpha_n^2+\frac{\nu}{1-2\nu}\frac{p^2}{c_1^2})e^{-\beta_{mn}Z}C_2+\alpha_n\gamma_{mn}e^{\gamma_{mn}Z}D_1\\&-\alpha_n\gamma_{mn}e^{-\gamma_{mn}Z}D_2]\cos\alpha_n x\cos\alpha_n y\\\bar{\sigma}_z=&\sum_{m=1}^{\infty}\sum_{n=1}^{\infty}[(-\beta_{mn}^2+\frac{\nu}{1-2\nu}\frac{p^2}{c_1^2})e^{\beta_{mn}Z}C_1\\&+(\beta_{mn}^2+\frac{\nu}{1-2\nu}\frac{p^2}{c_1^2})e^{-\beta_{mn}Z}C_2-\alpha_n\gamma_{mn}e^{\gamma_{mn}Z}D_1\\&+\alpha_n\gamma_{mn}e^{-\gamma_{mn}Z}D_2+\alpha_n\gamma_{mn}e^{\gamma_{mn}Z}E_1\\&-\alpha_m\gamma_{mn}e^{-\gamma_{mn}Z}E_2]\cos\alpha_m x\cos\alpha_n y\end{aligned} \quad (15)$$

Additionally, the strains can be expressed as follows:

$$\begin{aligned}\bar{\varepsilon}_x=&\frac{\partial\bar{u}}{\partial x}=\sum_{m=1}^{\infty}\frac{1}{2G}[(-\alpha_m^2)(C_1e^{\beta_{mn}Z}+C_2e^{-\beta_{mn}Z})\\&-\alpha_m\gamma_{mn}(E_1e^{\gamma_{mn}Z}-E_2e^{-\gamma_{mn}Z})]\cos\alpha_m x\cos\alpha_n y\\\bar{\varepsilon}_y=&\frac{\partial\bar{v}}{\partial y}=\sum_{m=1}^{\infty}\frac{1}{2G}[(-\alpha_n^2)(C_1e^{\beta_{mn}Z}+C_2e^{-\beta_{mn}Z})\\&+\alpha_n\gamma_{mn}(D_1e^{\gamma_{mn}Z}-D_2e^{-\gamma_{mn}Z})]\cos\alpha_m x\cos\alpha_n y\\\bar{\varepsilon}_z=&\frac{\partial\bar{w}}{\partial z}=\sum_{m=1}^{\infty}\frac{1}{2G}[\beta_{mn}^2(C_1e^{\beta_{mn}Z}+C_2e^{-\beta_{mn}Z})\\&+\alpha_n\gamma_{mn}(E_1e^{\gamma_{mn}Z}-E_2e^{-\gamma_{mn}Z})-\alpha_n\gamma_{mn}(D_1e^{\gamma_{mn}Z}\\&-D_2e^{-\gamma_{mn}Z})]\cos\alpha_m x\cos\alpha_n y\end{aligned} \quad (16)$$

Here, Δt is the sampling time, and the series are summed up to $(m, n)=(100, 100)$, where the strains and stresses lead to convergence.

2.2 Analysis of impact loading

In this section, Lagrange's classical theory and Hertzian contact theory are used to analyze impact loading in the case when measurement of impact loading is difficult, which consider local deformations by collisions between a steel ball and plate. So, the following impact loading coefficient can be derived as follows:

$$I_p P(\tau)^{2/3}=\tau-\int_0^{\tau}\int_0^{\xi}P(\eta)\,d\eta d\xi-\int_0^{\tau}P(\eta)\,d\eta \quad (17)$$

Here, $P(\tau)$ denotes the nondimensional impact

loading coefficient, $Ip=\frac{1}{m}\left(\frac{1}{V}\right)^{1/3}\left(\frac{1}{k}\right)^{2/3}\left(\frac{8D}{C_b}\right)^{5/3}$, m is the mass of the steel ball, V is the velocity of the ball, k is the contact coefficient of Hertz, D is the flexural rigid coefficient, and $C_b=\sqrt{\frac{D}{\rho h}}$.

Impact stresses can be analyzed by the inverse Laplace transform of Eq. (16) at an impact loading point, but it is hard to obtain the impact loading due to the nonlinear integral Eq. (17). Thus, the impact loading is obtained by the finite difference method from Eq. (17). If the impact loading can be approximated by analytic analyzable functions, impulsive stresses can be analyzed. Therefore, in this study, a method is presented to analyze impulsive stress.

The functional approximation of impact loading is suggested by the following equation in order to analyze impulsive stresses at a point of impact loading:

$$f(t)=Ate^{-\omega t} \tag{18}$$

After substituting the boundary condition given by Eq. (12) into Eq. (18), we can defermine the unknown coefficients (C_1, C_2, D_1, D_2, E_1, E_2).

3. Numerical Calculation

In this section, the equations of strain and stress components obtained with the Laplace transform, which were analyzed using the three-dimensional dynamic theory of elasticity, were found by the inverse Laplace transform, and impulsive stresses were analyzed. However, the inverse Laplace transform of three-dimensional dynamic theory of elasticity is difficult; thus, the numerical inverse Laplace transform is calculeted by the Fast Fourier transform:

$$(\varphi_0, \lambda_1, \lambda_2)_k=\frac{e^{\gamma k\Delta t}}{T}\sum_{n=0}^{N-1}(\varphi_0, \lambda_1, \lambda_2)_n \cdot e^{i2\pi n\frac{k}{N}}(k=0, 1, 2 \ldots N-1) \tag{19}$$

where $(\varphi_0, \lambda_1, \lambda_2)_k=(\varphi_0, \lambda_1, \lambda_2)_{t=k}\cdot\Delta t(\varphi_0, \lambda_1, \lambda_2)_n=(\varphi_0, \lambda_1, \lambda_2)_{p=r+in\Delta w}$, and $i=\sqrt{-1}$

Here, γ is the real part and ω the imaginary part of the Laplace transform parameter, N is the number of samples and T the sampling period, and $\Delta t=T/N$, $\Delta\omega=2\pi/T$ and $r>0$. Also, to improve precision and reduce computation time, length(x/h) and time (c_1/h) are treated as a nondimensional parameter. For numerical calculation the variable γ of Eq. (19) is set to $6/T$ (Krings, et al., 1979)

4. Experimental Apparatus and Method

In this experiment, to shoot with the required velocity, a horizontal-air-pressure impact testing apparatus was used, whose schematic diagram is shown in Fig. 2, and specimens are supported.

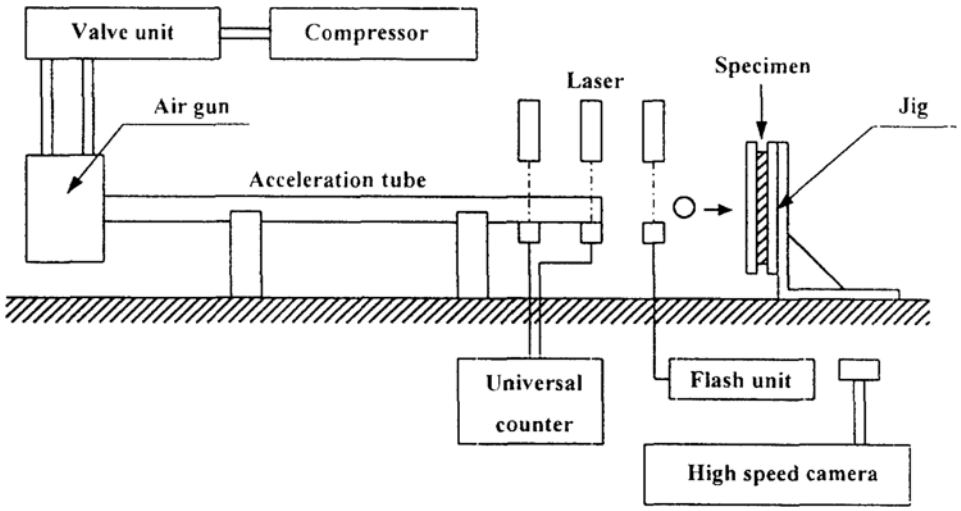

Fig. 2 Schematic diagram of impact apparatus

Impacts were made at the plate center at velocities a between 29 m/s and 130m/s. The impact velocity was obtained by varying air pressures on a compressor, and square plates made of glass with dimensions 300 mm × 300 mm × 2 mm, 3 mm, and 5 mm (width × length × thickness) were used. After bonding Rossete strain gauges on the center of the plate, we measure strain ε by impacting on the opposite side. When the strain ε_x is equal to the strain ε_y, we assume the impact is central.

The specimens are fixed supported at the edges, and strain is measured within the range before the glass plate is fractured. Also, material constants used in the numerical calculation were obtained by the three point bending test. It was determined that Young's modulus, E is 67.6 Gpa and the Poisson's ratio ν is 0.22. The velocity of the steel ball was measured just before impact by determining the time taken for it to pass two fine laser beams a known distance (10 mm) apart. Also, the steel-ball velocity after penetration was measured by using a high-speed camera, and the steel balls used in this test have diameters of 5 and 10 mm, respectively.

5. Comparison of Experimental and Analytical Results

5.1 Static fracture test

The results of the static fracture test are compared with numerically calculated solutions obtained using the three-dimensional dynamic theory of elasticity and the displacement potential theory at the concentrated impact loading point, with the Laplace transform parameter set to zero in this analysis.

Comparisons of experimental results with analytical solutions of Eq. (17) are shown in Fig. 3, where plates of thickness 2, 3 and 5 mm are fractured by static loads. In Fig. 3, symbol (×) denotes the fracture point. Experimental results agree well with analytical solutions as the plates become thicker; but for thinner plates, a difference between experimental and analytical results occurs due to plate bending stiffness.

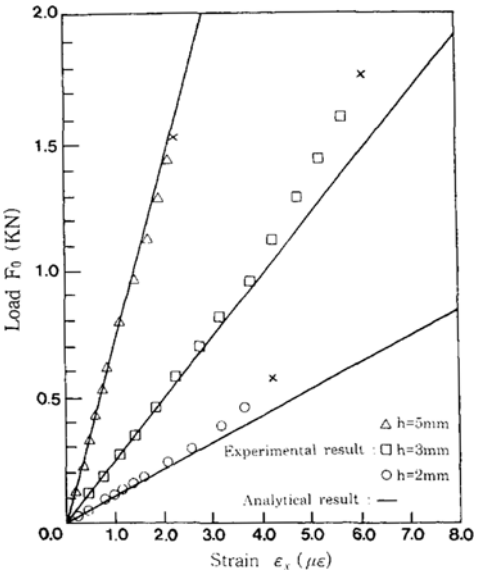

Fig. 3 Comparison of analytical results with experimental results of strain from the concentrated load point

5.2 Impact fracture test

First, to verify the analytical methods of implusive stresses using the three-dimensional theory and the approximation equation of impact loadng, the calculated results of the numerical inverse Laplace transform of strain Eq. (17) were compared with the results measured for strain at the point of concentrated impact loading.

In Fig. 4, a solid line shows the numerically calculated solution obtained by using $f(t)=At\exp(-\omega t)$. The dotted line shows the measurement of experimental results of strain. In Fig. 4, which shows a steel ball 20 mm in diameter with a velocity of 5m/sec impacting a 5 mm thick plate, numerically-calculated and experimental results are compared. By using the approximation equation $f(t)=At\exp(-\omega t)$, an error of approximately 14% occurs for the peak point of measuring strain as shown in Fig. 4.Also, times of peak points for strain waves appear at 28.12 μsec and 28 μsec, in that order. The experimental results agree with the analytical solution to a certain degree. Therefore, it is believed that the approximation equation $f(t)=At\exp(-wt)$, presented in this study is vaild in the application of stress analysis.

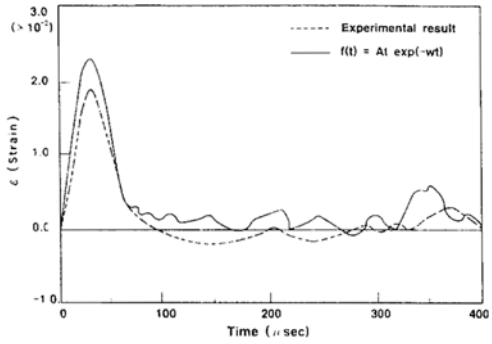

Fig. 4 Comparison of analytical solutions with experimental results with variations of time and strain at the impact point

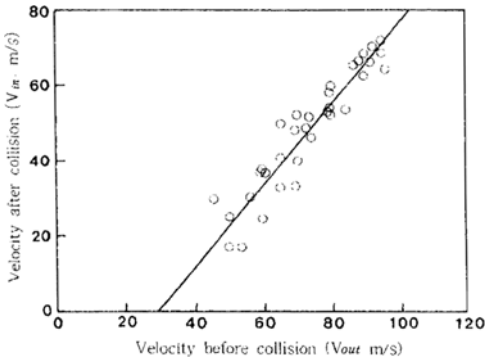

Fig. 5 Critical penetration velocity

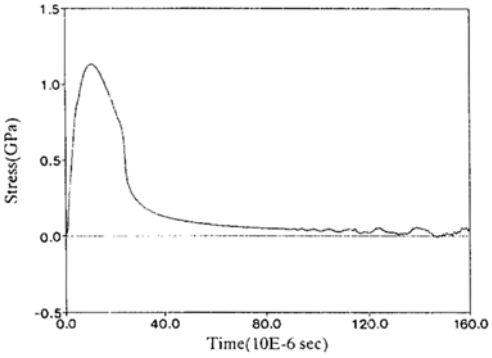

Fig. 6 Fracture strength at critical penetration velocity (steel sphere : ϕ 10, impact velocity : 29 m/sec, plate thickness : 3 mm)

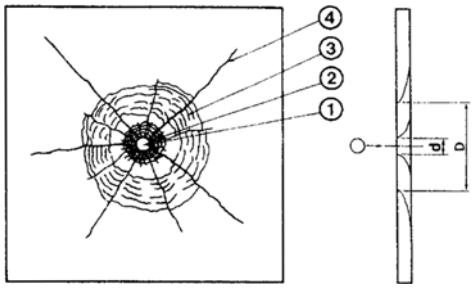

Fig. 7 Fracture patterns (① : Penetration hole, ②, ③ : Ring crack, ④ : Radial crack)

An impact testing apparatus was utilized as shown in Fig. 2. When the glass plates were broken, the penetration critical velocities were measured through repeated impact tests by using a high-speed camera. Also, Fig. 5 shows the results of the penetration test when a steel ball (ϕ 10 mm) was impacted on glass (thickness 3mm). The solid line of Fig. 5 is plotted with the method of least squares; the critical penetration velocity is 29 m/s, and the equation of the solid line is V_{out} = [1.067 V_{in}-31] m/s. The energy of the penetration velocity E_{crit} is 1.723 J.

As shown in Fig. 5, the variations of collision after/before velocity are constant regardless of velocity before collision, approximately 30 m/s. Fracture strength at which the glass plates cannot be penetration-fractured is obtained by substitution of the penetration critical velocity predicted in Fig. 5 and material properties of the steel ball and glass plates into Eqs. (12), (16) and (18). Figure 6 shows the analyzed solutions of stresses when a steel ball 10 mm in diameter is impacted on a glass plate 3 mm in thickness with an impact velocity of 29 m/s. So, the fracture strength at which penetration-fracture does not occur is 11.3269 GPa and the peak time is 10.9375 μsec.

Also, to consider how to change the patterns with variations in collision velocity, the plates of thickness 3 mm were impacted by a steel ball (ϕ =10 mm), and the impacted plate patterns are shown in Fig. 7. The fracture patterns consist of a penetration hole (①), ring cracks (②, ③) and radial cracks (④). The radial cracks almost reached the edges; inner parts of the ring cracks (②, ③) at the impact point are thinly fractured, and a hole (diameter d) of almost the same steel ball diameter is generated. The parts between ring cracks (②, ③) generally become flying debris. In the case of 100 m/s collision velocity, the fracture patterns are shown in Fig. 7; but with increasing velocity, ring cracks are not generated and the

length of the radial cracks becomes shorter than that of the radial cracks of Fig. 7. The inner diameter of the ring cracks becomes shorter with increasing velocity. The rough inner diameter is shown in Fig. 8 for variations in collision velocity.

Table 1 shows the fracture conditions when the plate of 3 mm thickness is impacted by a steel ball (ϕ=5 mm). With variations in collision velocity, crack patterns are as shown in Fig. 9. In the case of the steel ball (ϕ=5 mm) only, fracture conditions are observed because it is difficult to measure a steel ball velocity of mass 0.5 g after penetration. Especially, many tests were carried out within the range of the after/before penetration velocity. Penetration fracture occurs at approximately 94 m/s. The fracture does not occur before a collision velocity of 84 m/s, but within the range of 84~92 m/s, the radial cracks are generated from the impact point in static fracture patterns.

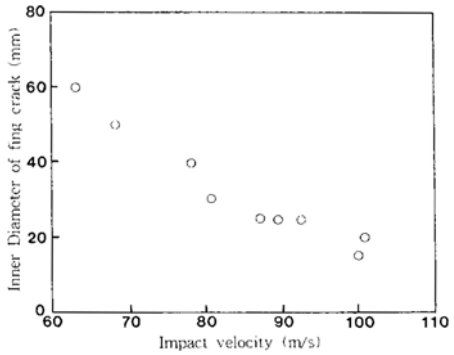

Fig. 8 Inner diameter of ring cracks with variations of collision velocity

By impacting a steel ball (ϕ=5 mm) on a plate from Table 1, the fracture-generated impact

Table 1 Fracture conditions

Impact velocity	Diameter of ring crack (mm)	Fracture form
0.93 J	-	Non-fracture
1.33 J	-	〃
1.40 J	-	〃
1.44 J	-	〃
1.64 J	-	〃
1.81 J	-	Radial crack, Non-penetration
2.08 J	-	〃
2.17 J	-	〃
2.27 J	50~100	Penetration
2.67 J	40~60	〃
3.11 J	40~50	〃
3.58 J	30~40	〃
4.02 J	15~20	〃
4.35 J	15	〃

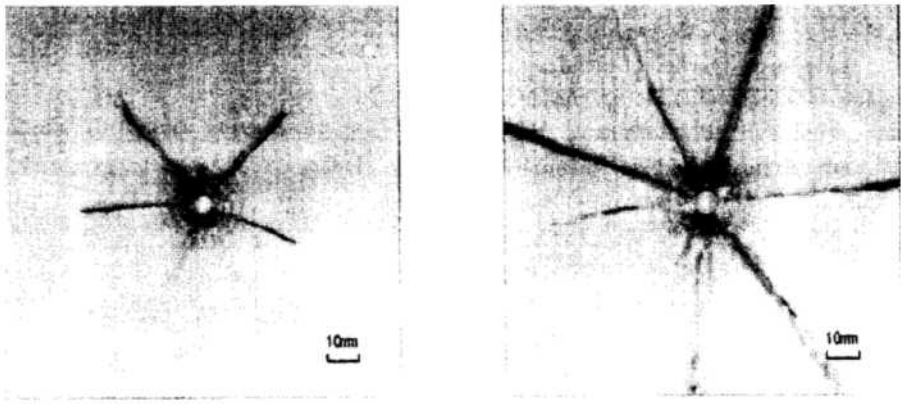

(a) 102 m/s (b) 94 m/s

Fig. 9 Crack patterns with variation of collision velocity (Steel ball: ϕ5 mm, plate thickness: 3 mm, impact velocities)

velocity is about 84 m/s (1.764 J) and the penetration-generated impact velocity is about 94 m/s (2.21 J). If the results are compared with the critical penetration energy in Fig. 5 (about 1.723 J in the case of a steel ball, ϕ 10 mm), the penetration-required kinetic energy for a steel ball of diameter 5 mm is increased by approximately 20% for a steel ball of diameter 10mm, and the fracture-required critical energy for a steel ball of diameter 5 mm is about 5% greater than that for a steel ball of diameter 10 mm. Thus, it is found that the fracture and penetration-required critical energy for a smaller steel ball is greater than for a larger steel ball. Also, if the magnitude of the ring cracks is compared with that of impact velocity as shown in Fig. 9 and Table 1, the diameter of the ring cracks and length of the ring cracks becomes shorter with an increase in impact velocity. For a penetration-initiated impact velocity of 94 m/s, Fig. 10 shows numerically calculated solutions of plate fracture strength in the case of impacting a steel ball (ϕ 5 mm) on a plate. The fracture strength of the plate is 4.9907 GPa, and the penetration-fractured strength of the plate is 5.0253 GPa. But, it is known that the above strength values appear smaller than 11.3269 GPa of penetration fracture strength within the range of critical-penetration velocity in the case of impacting a steel ball (ϕ 10 mm) on a plate. As the mass of the steel ball becomes smaller, the penetration-fracture strength decreases because the impulse of impacting a steel ball of thickness 10 mm (0.117605 N sec) is greater than that of impacting a steel ball of thickness 5 mm (0.05604 N sec) within the same range of each impact energy 1.6 J in the case of 28 m/s collision velocity using a ball diameter 10 mm and of 8 m/s collision velocity using a ball diameter 5 mm. Therefore, the penetration fracture is much more rapidly generated in the case of greater impulse even through the impact energies are the same as shown in Fig. 11 (Peak-point loading is 5666.518

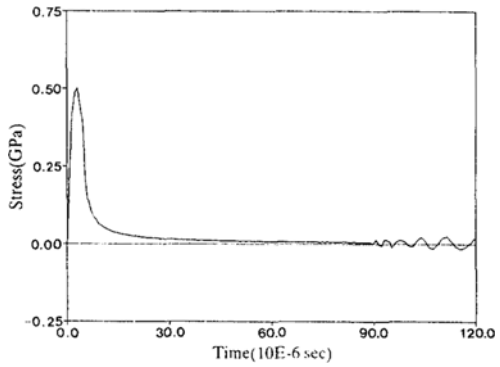

Fig. 10 Fracture strength velocity at penetration fracture initiation (ϕ5, h3, V=94 m/sec)

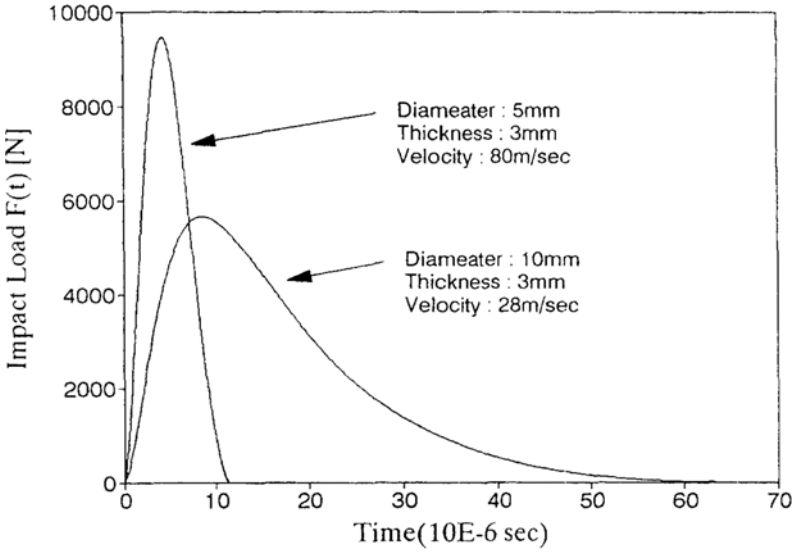

Fig. 11 Max. loading with the difference of masses of impactor (Impact energy E=1.6J)

N in the case of impacting a steel ball (ϕ 10 mm) with collision velocity 28 m/s and peak-point loading is 9459.742 N in the case of impacting a steel ball (ϕ 5 mm) with collision velocity 80 m/s and if compared with the above two kinds where impact energies are the same, peak value of impact loading appears to be greater for the smaller mass of steel ball).

6. Conclusions

The results obtained from this study are as follows:

(1) An analytical method to be approximated to the analyzable function is vaild, using the three-dimensional dynamic theory of elasticity and potential theory of displacement. Also, it is thought that this analysis can be applied to fracture strength estimation of brittle materials.

(2) Radial cracks are generated from the loading point regardless of plate thickness in the case of plates subjected to static loading. In the case of high-speed impact, dimensions of ring cracks become smaller and length of radial cracks becomes shorter with an increase in impact velocity.

(3) Kinetic change volume of collision after/before is constant regardless of velocities over the range of critical penetration velocities.

(4) Even though the impact energy is the same, the critical penetration energy increases with a decrease in impactor mass.

(5) Although the same impact energy is working, a greater penetration fracture is generated for a lighter impactor mass than for a heavier impactor mass, and the impulse of the lighter impacter mass appears greater than that of the heavier impactor mass. Therefore, the penetration fracture in the case of greater impulses is generated earlier regardless of the dimensions of impact loading.

References

Achenbach J. D., 1975, *Wave Propagation in Elastic Solids*, North-Holland Publishing Co., New York, p. 67.

Chao C. C. and Tung T. P., 1989, "Step Pressure and Blast Response of Clamped Orthotropic Hemispherical Shells," *Int. J. Impact Engng.*, Vol. 8, No. 3, pp. 191~207.

Ganebasi C., Yueoga N. and Paeski O., 1993, "Impact Analysis of CRT", *Strength of Materials of JSME*, 11, pp. 423~427.

Goldsmith, W, 1990, *Impact*, Edward Arnold, London, pp. 82~91.

Holian Kathleen S., 1990, "Hydrondynamics Code Calculation of Debris Clouds Produced by Ball-Plate Impacts," *Int. J. Impact Engng.*, Vol. 10, pp. 231~239.

Hondou G., Noudaka S. and Goarma H., 1978, "Failure Mechanism of Braun Tube for Color TV," *JSME(I)*, Vol. 44, No. 386, pp. 3363~3370.

Johnson W., 1972, *Impact Strength of Materials*, Edward Arnold, London p. 106.

Kim Y. B., Lee S. Y. and Kim D. C., 1993, "A Study for Structure Improvement of Large Size TV Using Impact Simulation," *Proceedings of the KSME Autumn Annual Meeting '93*, Vol. (I), pp. 81~84, in Korean.

Kishimoto K., Aoki S. and Sakata M., 1980, "Simple Formula or Dynamic Stress Intensity Factor of Precracked Charpy Specimen," *Engng. Fract. Mech.*, 13, p. 501.

Krings W. and Waller H., 1979, "Contribution to the Numerical Treatment of Partial Differential Equations with the Laplace Transformation - An Application of the Algorithm of the Fast Laplace Transformation," International Journal for Numerical Method in Engineering, Vol. 14, p. 1186,

Nakahara I., 1977, *Theory of Applied Elasticity*, Jitsu-Kyu Publishing Co., Tokyo, p. 207.

Ni Hei-Shu, 1985, *Theory of Modern Elasticity*, OMU Publishing Co., Tokyo, pp. 26~34.

Ujihashi S. Y., Adachi T. H., Inoue H. T. and Matsumoto H. Y., 1986, "An Analytical and Experimental Study of Impulsive Stresses in a Glass Plate Subjected to the Transverse Impact of Steel Balls," *JSME(A)*, Vol. 52, No. 474, pp. 505~531.

Wang Xiaowei and Yew Ching H., 1989, "Hypervelocity Impact of Two Spheres," *Int. J.*

Impact Engng., Vol. 8, No. 3, pp. 229~240.

Yang I. Y., 1988, "An Analytical Study of Impulsive Stresses in a Square Plate Subjected to a Concentrated Impact Using the Three-Dimensional Dynamic Theory of Elasticity," Ph. D. Thesis. Chonnam National University, pp. 5~18, in Korean.

Yang. I. Y., Kim. S. K. and Yang. I. Y., 1994 "An Analytical and Experimental Study of Impulsive Stress of Square Plates at an Impact Loading Point by the 3-Demensional Dynamic Theory of Elasticity," *KSME*, Vol. 8, No. 3, pp. 303~313